Optical tweezers absolute calibration

R S Dutra[1,2,3], N B Viana[2,3], P A Maia Neto[2,3] and H M Nussenzveig[2,3]
[1] *Instituto Federal de Educação, Ciência e Tecnologia, Rua Sebastião de Lacerda, Paracambi, RJ, 26600-000, Brasil*
[2] *LPO-COPEA, Instituto de Ciências Biomédicas, Universidade Federal do Rio de Janeiro, Rio de Janeiro, RJ, 21941-590, Brasil and*
[3] *Instituto de Física, Universidade Federal do Rio de Janeiro, Caixa Postal 68528, Rio de Janeiro, RJ, 21941-972, Brasil*
(Dated: June 30, 2014)

Optical tweezers are highly versatile laser traps for neutral microparticles, with fundamental applications in physics and in single molecule cell biology. Force measurements are performed by converting the stiffness response to displacement of trapped transparent microspheres, employed as force transducers. Usually, calibration is indirect, by comparison with fluid drag forces. This can lead to discrepancies by sizable factors. Progress achieved in a program aiming at absolute calibration, conducted over the past fifteen years, is briefly reviewed. Here we overcome its last major obstacle, a theoretical overestimation of the peak stiffness, within the most employed range for applications, and we perform experimental validation. The discrepancy is traced to the effect of primary aberrations of the optical system, which are now included in the theory. All required experimental parameters are readily accessible. Astigmatism, the dominant effect, is measured by analyzing reflected images of the focused laser spot, adapting frequently employed video microscopy techniques. Combined with interface spherical aberration, it reveals a previously unknown window of instability for trapping. Comparison with experimental data leads to an overall agreement within error bars, with no fitting, for a broad range of microsphere radii, from the Rayleigh regime to the ray optics one, for different polarizations and trapping heights, including all commonly employed parameter domains. Besides signalling full first-principles theoretical understanding of optical tweezers operation, the results may lead to improved instrument design and control over experiments, as well as to an extended domain of applicability, allowing reliable force measurements, in principle, from femtonewtons to nanonewtons.

arXiv:1406.7176v1 [physics.optics] 27 Jun 2014

I. INTRODUCTION

Optical tweezers (OT), invented in 1986 [1], are laser traps for neutral microscopic particles, with a vast range of applications in physics and biology: a 2006 review [2] lists $\sim 10^3$ publications. Recent applications to fundamental physics include an experimental realization of Szilard's demon [3] and the first experimental proof of Landauer's principle [4]. In cell biology, OT have paved the way to pioneering quantitative measurements of basic interactions in living cells, "one molecule at a time" [5, 6].

For biological applications, one employs near-infrared laser light, within a transparency window for the water contained in cells, to avoid heat damage. A transparent microsphere is employed as a handle and force transducer. The microsphere is pulled toward the diffraction-limited laser focus by the gradient force, which must overcome the opposing radiation pressure, thus requiring a strongly focused beam. The beam is focused through the microscope objective. To maintain the live biological sample, it is usually immersed in water solutions, within a chamber with controlled temperature and carbon dioxide pressure. For a schematic diagram of a typical set-up see [7].

The object of interest is attached to the trapped microsphere, through which the force is applied, usually transverse to the beam. For sufficiently small microsphere displacements from equilibrium, the response is linear both in displacement and in laser power, so that it suffices to calibrate the transverse trap stiffness per unit power, measuring the displacement to determine the force.

Stiffness calibration is usually based on comparisons with fluid drag forces [8] or on detection of thermal fluctuations [9] by assuming a known drag coefficient. Alternatively, measuring the power spectra under a sinusoidal motion of the microscope translational stage allows for an independent calibration of the drag force on the trapped particle [10]. In cell biology, forces may need to be measured under complicated boundary conditions, at micrometer distances from the bottom of the sample chamber. Results at different laboratories can disagree even by an order of magnitude (e. g., [11]).

In the present work, we demonstrate an absolute calibration of stiffness, based on a careful control of all relevant trap parameters [12] and on an accurate realistic theory of the trapping force, yielding the stiffness in terms of experimentally accessible data. The basic ingredients of such a theory are the description of the strongly focused laser beam and of its interaction with the microsphere.

Early treatments [1] of the interaction were confined to the Rayleigh regime (microsphere radius a below $0.1\,\mu$m), in which the stiffness grows like a^3, and to the geometrical optics limit [13, 14] $a \gg \lambda$, where $\lambda \sim 1\,\mu$m is the laser wavelength. In usual experiments, a is $\lesssim 1\,\mu$m, in the Mie regime. In the widely referenced "generalized Lorenz-Mie theory" [15, 16], however, the trapping beam was described in terms of perturbative corrections

to a paraxial Gaussian model, which has been shown [17] to be an incorrect representation of a strongly focused beam. A proper representation of such a beam [14] is the electromagnetic generalization [18] of Debye's classic scalar model [19]. A more detailed overview of other proposals is given in [12].

The generalized Debye representation, combined with Mie theory, and taking due account of the Abbe sine condition, was first applied to the axial stiffness [20]. This MD (Mie-Debye) theory predicts rapid oscillations in a/λ, arising from interference between contributions from the sphere edges for spectral angular components. Related oscillations have been detected in optical trapping of water droplets [21]. As is expected in semiclassical scattering [22], averaging over oscillations, for $a \gg \lambda$, yields the geometrical optics result, which decays asymptotically like $1/a$, as follows from dimensional analysis. Previous theories did not show oscillations and had incorrect asymptotic behavior.

The extension of MD theory to the more relevant transverse stiffness [23], with similar features, differed from available experimental data by an apparent overall displacement. This was traced back to its disregard of interface spherical aberration, the defocussing of the laser beam by refraction at the interface between the glass slide and the water in the sample chamber [24]. Inclusion of this effect led to the MDSA (Mie-Debye-Interface Spherical Aberration) theory [12].

Extensive experimental tests of the MDSA theory for different OT setups [12, 25, 26] showed good agreement with its predictions in the range $a > \lambda$, for the trapping threshold, location of the stiffness peak, stiffness degradation with height in the sample chamber, and "hopping" between multiple equilibrium points. Recent extensions include modeling counterpropagating dual-beam [27] and aerosol optical traps [28]. However, under the usual conditions of an overfilled high numerical aperture (NA) objective, MDSA leads to a huge overestimation of the stiffness in the interval $a \lesssim \lambda/2$, where the predicted stiffness is maximal. This is precisely the size domain of greatest importance for practical applications, thus compromising the validity of MDSA for absolute calibration. It was conjectured in [12] that additional optical aberrations of the microscope objective could be responsible for the stiffness reduction, by degrading the focus.

In the present work, we investigate in detail the effects of all primary aberrations on the optical trapping force. Building on our previous theoretical work, we develop a new model, denoted as MDSA+, that takes into account the presence of primary aberrations of the focused trapping beam in addition to the interface spherical aberration.

We show that one additional optical aberration, astigmatism, is the main effect responsible for the transverse stiffness degradation in the range $a \lesssim \lambda/2$. We independently characterize the astigmatism of our OT setup and plug the results into MDSA+ theory. We find agreement with the experimental data within error bars, with no fitting procedure. The success of such blind comparison is of particular importance, given that astigmatism is always present to some degree in typical OT setups (see for instance [29]). It also demonstrates that absolute calibration of the trap stiffness can be achieved, provided that all relevant experimental parameters, including the astigmatism, are carefully characterized.

Preliminary results for the case of circular polarization were briefly reported in Ref. [30]. Here we present a comprehensive account of the effects of all primary aberrations on the optical force field. We choose to present the most common case of linear polarization so as to provide more useful guidelines for typical optical tweezers setups.

The paper is organized as follows: in Sec. II we develop MDSA+ and consider numerical examples, taking each primary aberration separately (explicit formulas are given in Appendix A). Sec. III is dedicated to the characterization of astigmatism in our typical OT setup. We compare experimental data with theoretical predictions for the trap stiffness in Sec. IV. Concluding remarks are presented in Sec. V. The main conclusion is that absolute calibration of optical tweezers has finally been achieved and that it should lead to significant practical consequences. Appendix B provides a short guide to the implementation of absolute calibration.

II. MDSA+ THEORY OF THE OPTICAL FORCE IN THE PRESENCE OF ABERRATIONS

A. General formalism

In this section, we derive formal results for the optical force in the presence of aberrations. In the typical optical tweezer setup, the trapping laser beam is focused by a high numerical-aperture (NA) oil-immersion objective into a sample region filled with water. The effect of the spherical aberration introduced by the glass-water planar interface was already analyzed in detail in Ref. [26]. Here we also take into account additional optical aberrations introduced by the objective itself and by optical elements along the optical path before the objective.

We assume that the trapping laser beam at the entrance port (aperture radius R_0) of the infinity-corrected microscope objective (focal length f) has amplitude E_p, waist w_0 and is linearly polarized along the x-axis. We employ the Seidel formalism for the aberrations [31]. Among the Seidel primary aberrations, we expect field curvature and distortion to keep the three-dimensional intensity distribution around the focal region approximately unchanged, except for a global spatial translation (displacement theorem [31]). Thus, we focus on the effects of spherical aberration, coma and astigmatism.

To include these three primary aberrations into our theoretical model, we introduce the corresponding phase for each plane wave component associated to a given angle (θ, φ) (in spherical coordinates) into the Debye-type angular spectrum representation of the focused beam.

We assume that the objective satisfies the usual sine condition and we write the focused electric field as (origin at the paraxial focus)

$$\mathbf{E}(\mathbf{r}) = E_0 \int_0^{2\pi} d\varphi \int_0^{\theta_m} d\theta \sin\theta \sqrt{\cos\theta} e^{-\gamma^2 \sin^2\theta} T(\theta) \times e^{i[\Phi_{\mathrm{g-w}}(\theta)+\Phi_{\mathrm{add}}(\theta,\varphi)]} e^{i\mathbf{k}_{\mathrm{w}}\cdot\mathbf{r}} \hat{\mathbf{x}}'(\theta_{\mathrm{w}},\varphi_{\mathrm{w}}), \quad (1)$$

with $\gamma = f/w_0$ and $E_0 = -(ikf/2\pi)E_p \exp(ikf)$. The wavevector in the sample region has modulus $k_{\mathrm{w}} = Nk$ where $N = n_{\mathrm{w}}/n$ is the relative refractive index for the glass-water interface and k is the wavenumber in the glass medium of refractive index n. The direction of $\mathbf{k}_{\mathrm{w}}$ is defined by the spherical coordinates $(\theta_{\mathrm{w}}, \varphi_{\mathrm{w}})$, where $\theta_{\mathrm{w}} = \sin^{-1}(\sin\theta/N)$ (refraction angle) and $\varphi_{\mathrm{w}} = \varphi$. The Fresnel refraction amplitude

$$T(\theta) = \frac{2\cos\theta}{\cos\theta + N\cos\theta_{\mathrm{w}}} \quad (2)$$

accounts for the amplitude transmission across the interface. More importantly, Eq. (1) contains the phase

$$\Phi_{\mathrm{g-w}}(\theta) = k\left(-\frac{L}{N}\cos\theta + NL\cos\theta_{\mathrm{w}}\right), \quad (3)$$

proportional to the distance L between the paraxial focus and the planar interface, accounting for the spherical aberration introduced by refraction at the glass-water interface. The unit vector $\hat{\mathbf{x}}'(\theta_{\mathrm{w}},\varphi_{\mathrm{w}})$ in (1) is obtained from $\hat{\mathbf{x}}$ by rotation with Euler angles $(\varphi_{\mathrm{w}}, \theta_{\mathrm{w}}, -\varphi_{\mathrm{w}})$:

$$\hat{\mathbf{x}}' = \cos\varphi_{\mathrm{w}}\,\hat{\boldsymbol{\theta}}_{\mathrm{w}} - \sin\varphi_{\mathrm{w}}\hat{\boldsymbol{\varphi}}_{\mathrm{w}}.$$

When the numerical aperture (NA) is larger than n_{w} (for instance for the popular NA = 1.4 objectives), part of the angular spectrum exceeds the critical angle $\theta_{\mathrm{cr}} = \sin^{-1}(N)$ for total internal reflection, producing evanescent waves in the sample region. Here we assume that the trapped microsphere is several wavelengths away from the interface, allowing us to neglect the contribution of the evanescent sector. Thus, we limit the integration in (1) to

$$\theta_m = \min\{\theta_{\mathrm{cr}}, \theta_0 \equiv \sin^{-1}(\mathrm{NA}/n)\}.$$

The main novelty in Eq. (1) is the phase

$$\frac{\Phi_{\mathrm{add}}(\theta,\varphi)}{2\pi} = A'_{\mathrm{sa}}\left(\frac{\sin\theta}{\sin\theta_0}\right)^4 + A'_{\mathrm{c}}\left(\frac{\sin\theta}{\sin\theta_0}\right)^3 \cos(\varphi-\phi_{\mathrm{c}}) + A'_{\mathrm{a}}\left(\frac{\sin\theta}{\sin\theta_0}\right)^2 \cos^2(\varphi-\phi_{\mathrm{a}}), \quad (4)$$

containing the relevant primary aberrations in the optical system (objective included). In (4), A'_{sa}, A'_{c} and A'_{a} represent the amplitudes of system spherical aberration (in addition to the one introduced by the glass-water interface), coma and astigmatism, respectively. The index sa is meant to distinguish optical system (objective and remaining optical elements, e.g., telescopic system) spherical aberration from interface spherical aberration, already included in MDSA. The coma and astigmatism axes are defined by the angles ϕ_{c} and ϕ_{a}, measured with respect to the x axis in the image space of the objective.

The scattered fields for each plane wave component in (1) are written in terms of Wigner rotation matrix elements $d^j_{m,m'}(\theta_{\mathrm{w}})$ [32] and Mie coefficients a_j and b_j for electric and magnetic multipoles, respectively [33]. The integer variables $j \geq 1$ and $m = -j, ..., j$ represent the total angular momentum J^2 (eigenvalues $j(j+1)$) and its axial component J_z, respectively. After expanding the focused field (1) into multipoles, we evaluate the integral over the azimuth angle φ and use Graf's generalization of Neumann's addition theorem for cylindrical Bessel functions $J_n(x)$ [34]. A partial-wave (multipole) representation for the optical force is then derived from the Maxwell stress tensor [35]. Since the optical force $\mathbf{F}$ is proportional to the laser beam power P at the sample region, it is convenient to define the dimensionless vector efficiency factor [14]

$$\mathbf{Q} = \frac{\mathbf{F}}{n_{\mathrm{w}}P/c}, \quad (5)$$

where c is the speed of light in vacuum. The cylindrical components of $\mathbf{Q}$ are given in Appendix A, in terms of the incident field multipole coefficients

$$G^{(\sigma)}_{jm}(\rho,\phi,z) = \int_0^{\theta_m} d\theta \sin\theta\sqrt{\cos\theta}\, e^{-\gamma^2\sin^2\theta}\, T(\theta)\, d^j_{m,\sigma}(\theta_{\mathrm{w}})\, g^{(\sigma)}_m(\rho,\phi,\theta) \exp\{i[\Phi_{\mathrm{g-w}}(\theta) + \Psi_{\mathrm{add}}(\theta) + k_{\mathrm{w}}\cos\theta_{\mathrm{w}} z]\} \quad (6)$$

where $\sigma = \pm 1$ denotes the photon helicity. The phase

$$\Psi_{\mathrm{add}}(\theta) = 2\pi A'_{\mathrm{sa}}\left(\frac{\sin\theta}{\sin\theta_0}\right)^4 + \pi A'_{\mathrm{a}}\left(\frac{\sin\theta}{\sin\theta_0}\right)^2 \quad (7)$$

accounts for additional spherical aberration and a residual field curvature arising from the Seidel astigmatism. The

anisotropy introduced by astigmatism and coma is contained in the function

$$g_m^{(\sigma)}(\rho,\phi,\theta) = e^{i(m-\sigma)\alpha} \sum_{s=-\infty}^{\infty} (-i)^s J_s\left(\pi A'_{\rm a}\frac{\sin^2\theta}{\sin^2\theta_0}\right) J_{2s+m-\sigma}(|\mathcal{Z}|)\, e^{2is(\alpha+\phi_{\rm a}-\phi)} \tag{8}$$

where the coma parameters define the complex quantity

$$\mathcal{Z} = k\rho\sin\theta - 2\pi A'_{\rm c}\frac{\sin^3\theta}{\sin^3\theta_0}e^{-i(\phi_{\rm c}-\phi)} = |\mathcal{Z}|\, e^{i\alpha}. \tag{9}$$

Most numerical examples discussed in this paper involve the trap stiffness rather than the force itself. Except in the case of coma, we compute the stiffness by first taking the spatial derivative (usually with respect to ρ) of the partial-wave series for the relevant force component in order to obtain the partial-wave series for the trap stiffness itself, which is then numerically evaluated.

B. Numerical results

In all numerical examples discussed in this section, we take a typical setup often used in quantitative applications. We consider a polystyrene (refractive index 1.57) microsphere of radius $a = 0.26\,\mu$m immersed in water (index $n_{\rm w} = 1.32$) trapped by a Nd:YAG laser beam (wavelength $\lambda = 1.064\,\mu$m, waist $w_0 = 4.2\,$mm). The beam is focused by an oil-immersion (glass index $n = 1.51$) objective of NA = 1.4 and entrance aperture radius $R_0 = 3.5$ mm.

The formalism presented in Sec. II A allows one to consider the joint effects of astigmatism, coma and spherical aberration. We begin by considering each primary aberration separately in order to grasp their physical effects on the optical force field. We start with the simplest one: spherical aberration.

1. *Joint interface and system spherical aberration*

In this sub-section, we assume that the optical setup contains only spherical aberration: $A'_{\rm a} = A'_{\rm c} = 0$. In order to control the amount of interface spherical aberration, we need to evaluate the distance L between the paraxial focus and the glass slide [see Eq. (3)], which is not directly accessible in our calibration experiments. Experimentally, we start from the configuration in which the bead touches the glass slide at the bottom of the sample chamber and then displace the inverted objective upward by a known distance d. Hence the paraxial focus is displaced vertically from its initial position by a distance Nd. We mimic this experimental procedure in the following way. We first compute the initial distance between the paraxial focus and the glass slide L_0 by using the condition that the bead is initially at equilibrium just touching the glass slide. Then we take $L = L_0 + Nd$.

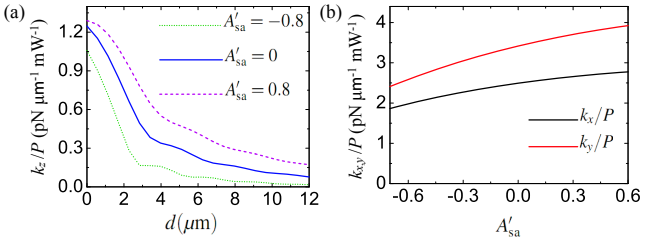

FIG. 1: (Color online) Trap stiffness dependence on system spherical aberration. a) Axial stiffness per unit power as a function of the objective upward displacement d, for different values of the system spherical aberration amplitude $A'_{\rm sa}$. b) Transverse stiffnesses per unit power as a function of $A'_{\rm sa}$ for a fixed objective displacement $d = 3\,\mu$m. The stiffness is larger along the direction perpendicular (y direction) to the laser beam polarization at the objective entrance.

We consider the joint effect of the interface and system spherical aberrations on the trap stiffness. We first compute the equilibrium position $z_{\rm eq}$ by solving the implicit equation $Q_z(\rho = 0, z_{\rm eq}) = 0$. The resulting position is slightly above the diffraction focus because of radiation pressure, and below the paraxial focus for $A'_{\rm sa} \leq 0$ (the ratio between the displacement of the equilibrium position and d is usually known as 'effective focal shift' [36]). We derive partial-wave series for the dimensionless force derivatives from the results given in Appendix A and then take $\rho = 0$, $z = z_{\rm eq}$ to calculate the axial stiffness per unit power; similarly for the transverse stiffness k_ρ.

In Fig. 1(a), we plot the axial trap stiffness k_z as a function of the objective upward displacement d, for different values of the system spherical aberration amplitude $A'_{\rm sa}$. The solid line, representing the case with only interface spherical aberration, is very similar to the result found in Ref. [36]. As expected, increasing the focal height with respect to the glass slide degrades the focal region, leading to a severe axial stiffness reduction. Since the interface spherical aberration is negative (i.e. the real wavefront is ahead of the ideal spherical reference wavefront), a positive $A'_{\rm sa}$ leads to a partial compensation of the interface effect, as shown in Fig. 1(a), whereas a negative $A'_{\rm sa}$ enhances the focal region degradation.

The transverse stiffness per unit power k_ρ is less sensitive but also decreases with the trapping height. Here again a positive system spherical aberration partially compensates the effect of the interface one. In Fig. 1b, we plot k_ρ as a function of $A'_{\rm sa}$ taking $d = 3\,\mu$m. The stiffness is larger along the direction perpendicular to the incident polarization ($\phi = \pi/2$ corresponding to k_y) be-

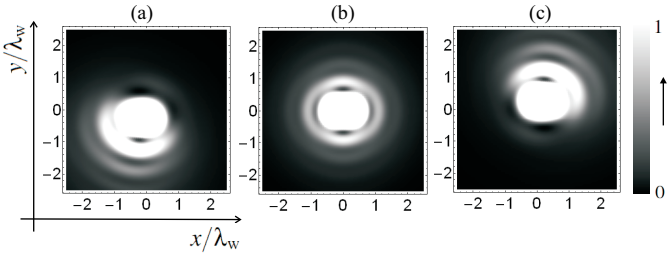

FIG. 2: Theoretical relative electric energy density $E^2/E^2_{\max}$ on the plane $z = z_{\rm eq}$ in the presence of coma ($\lambda_{\rm w} = \lambda/n_{\rm w}$ is the wavelength in the sample medium). We take $\phi_{\rm c} = \pi/3$ and (a) $A'_{\rm c} = -0.93$, (b) $A'_{\rm c} = 0$ and (c) $A'_{\rm c} = 0.93$. Note that the non-paraxial coma-free focused spot (b) is elongated along the polarization direction x of the laser beam at the objective entrance port [18].

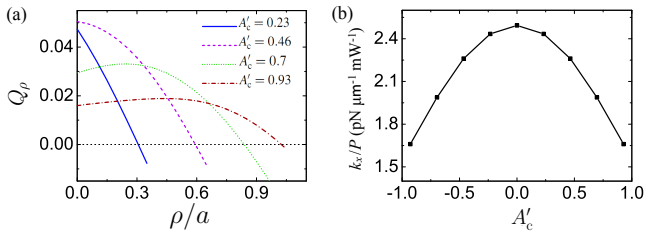

FIG. 3: (Color online) Optical trap with coma. (a) Dimensionless radial force Q_ρ as a function of the cylindrical coordinate ρ along the coma axis $\phi = \phi_{\rm c}$. The point of equilibrium is off axis. (b) Transverse trap stiffness per unit power k_x/P along the direction parallel to the incident polarization as a function of the coma amplitude.

cause the electric energy density gradient is larger along this direction [18].

2. *Coma*

When we add coma to our setup, the equilibrium position is no longer along the z-axis, because the point of maximum energy density is displaced away from the axis along the direction set by the coma axial direction $\phi = \phi_{\rm c}$ on the xy plane. This is illustrated in Figs. 2(a) and 2(c), where we plot the electric energy density divided by its maximum value $E^2/E^2_{\max}$ at the plane $z = z_{\rm eq}$ corresponding to the axial equilibrium position ($E^2 = |\mathbf{E}|^2$ is the electric field square modulus). We also show the spot with zero coma for comparison [2(b)]. For all numerical examples presented in Figs. 2 and 3, we take the coma axial direction at $\phi_{\rm c} = \pi/3$ and fix the distance between the paraxial focus and the glass slide to be $L = 2.9\,\mu$m.

We find that the equilibrium position also lies along the coma axis in general (and not only in the Rayleigh regime), regardless of the polarization direction at the objective entrance port. In order to determine the full equilibrium position, we first find the coordinate $z = \bar{z}(\rho)$ yielding axial equilibrium as we change the lateral position ρ by solving the implicit equation

$$Q_z(\rho, \phi = \phi_{\rm c}, \bar{z}(\rho)) = 0. \qquad (10)$$

We then plot $Q_\rho(\rho, \phi = \phi_{\rm c}, \bar{z}(\rho))$ as a function of ρ for different values for the coma amplitude $A_{\rm c}$ in Fig. 3a. The distance $\rho_{\rm eq}$ between the equilibrium position and the z-axis is given by the intersection between the different curves and the horizontal dashed line $Q_\rho = 0$. Fig. 3a shows that the equilibrium point is displaced away from the z-axis as we increase the coma amplitude, as expected. Moreover, the figure shows that the equilibrium point is radially stable. By analyzing the dimensionless force components Q_z and Q_ϕ, we find that the equilibrium point is also stable with respect to axial and tangential displacements.

As in the coma-free simulations presented in Ref. [23], Fig. 3a simulates experiments where a transverse Stokes drag force $F_{\rm Stokes}$ is applied to the trapped microsphere, provided that the Stokes force is parallel to the coma axis. In this case, the new radial equilibrium position can be read from Fig. 3 by taking the value of ρ corresponding to $Q_\rho = -cF_{\rm Stokes}/(n_{\rm w}P)$. Note that each value of ρ corresponds to a different axial coordinate $\bar{z}(\rho)$ defined by (10), for the microsphere is also displaced along the axial direction when applying the lateral Stokes force [14] as demonstrated in Ref. [37].

The Stokes calibration provides perhaps the simplest method for measuring the transverse trap stiffness. The radial stiffness k_ρ corresponds to the slopes shown in Fig. 3a at $\rho = \rho_{\rm eq}$. It is already clear from this figure that k_ρ decreases with increasing coma amplitude.

It is more common, however, to measure the transverse stiffnesses parallel (k_x) or perpendicular (k_y) to the polarization axis. We calculate k_x for a focused beam with coma from the numerical evaluation of the slope of Q_x in the neighborhood of the point of equilibrium. In Fig. 3b, we plot k_x per unit power as a function of $A'_{\rm c}$ showing that the stiffness reduction does not depend on its sign. This symmetry also follows from (4): changing the sign of $A'_{\rm c}$ is equivalent to shifting $\phi_{\rm c} \to \phi_{\rm c} + \pi$, which amounts to rotating the energy density profile by π, as illustrated by Figs. 2a and 2c. The equilibrium position is then displaced along the opposite direction but the stiffness remains the same. These results are in qualitative agreement with the experimental data presented in Ref. [29].

3. *Astigmatism*

The phase correction corresponding to astigmatism, on the other hand, has a different symmetry property under the change of sign of its amplitude, so that the stiffness is not an even function of $A'_{\rm a}$. According to (4), when $\phi_{\rm a} \to \phi_{\rm a} + \pi/2$ the astigmatism phase correction changes sign and yields a residual proportional to ρ^2, which corresponds to curvature of field. The latter produces essen-

tially a displacement of the energy density profile along the z-axis [31], with a negligible effect on stiffness. The transformation $A'_{\rm a} \rightarrow -A'_{\rm a}$ is therefore approximately equivalent to rotating the astigmatism axis by $\pi/2$ [38].

This is verified by the numerical calculations presented in Fig. 4, where we plot the transverse stiffnesses per unit power parallel (k_x/P) and perpendicular (k_y/P) to the incident polarization as functions of $A'_{\rm a}$. We take a fixed objective displacement $d = 3\,\mu$m and the astigmatism axis orientations $\phi_{\rm a} = 0$ (4a), $\phi_{\rm a} = \pi/4$ (4b), and $\phi_{\rm a} = \pi/2$ (4c). The values for $A'_{\rm a} = 0$, indicated by vertical dashed lines, are of course the same for the three plots and show that the stiffness is larger along the direction perpendicular to the incident polarization as expected, since the energy density spot at the focal plane in the non-paraxial regime is elongated along the incident polarization direction x in the stigmatic case [18], as shown by Fig. 5a.

By changing the spot shape on the xy plane, astigmatism produces a strong effect on the transverse stiffnesses and in particular on their relatives values. The relative electric energy density at the plane $z = z_{\rm eq}$ is shown in Fig. 5, with the astigmatism axis at $\phi_{\rm a} = 0$. In order to understand the results shown in Figs. 4 and 5, we have to bear in mind that radiation pressure pushes the equilibrium point to a plane above the diffraction focus (circle of least confusion). For that reason, when taking $\phi_{\rm a} = 0$ (Fig. 4a) the spot on the equilibrium plane $z = z_{\rm eq}$ gradually becomes more elongated along the y axis as we increase $A'_{\rm a}$, as illustrated by Fig. 5. As a consequence, k_y decreases very fast, whereas k_x is initially constant and then starts to decrease as well, since larger values of astigmatism will ultimately degrade the energy density gradient also along x. For $A'_{\rm a} = 0.44$, astigmatism yields an exact cancelation of the non-paraxial effect on the spot shape and then we have $k_x = k_y$. Beyond that point, astigmatism dominates and the spot becomes more elongated along the y direction, yielding $k_x > k_y$.

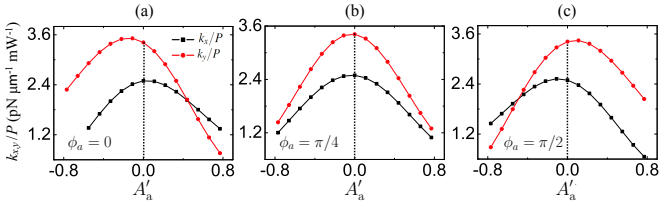

FIG. 4: (Color online) Transverse stiffnesses per unit power k_x/P and k_y/P as functions of the astigmatism amplitude $A'_{\rm a}$ for axis orientations (a) $\phi_{\rm a} = 0$; (b) $\phi_{\rm a} = \pi/4$ and (c) $\phi_{\rm a} = \pi/2$. The vertical dashed lines indicate the values in the stigmatic case. The x axis ($\phi = 0$) corresponds to the trapping laser beam polarization at the objective entrance.

On the other hand, the gradual introduction of a negative astigmatism ($A'_{\rm a} < 0$) makes the spot still more elongated along the polarization direction x, reinforcing the gradient along y for moderate values of $A'_{\rm a}$. Thus, k_y is slightly increased by the introduction of a small negative astigmatism as shown by Fig. 4a. Larger values of $A'_{\rm a}$ will ultimately degrade both k_x and k_y.

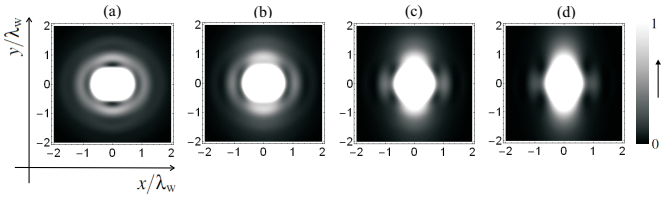

FIG. 5: Theoretical relative electric energy density $E^2/E^2_{\rm max}$ on the plane $z = z_{\rm eq}$ in the presence of astigmatism (same conventions as Fig. 2). We take $\phi_{\rm a} = 0$ and (a) $A'_{\rm a} = 0$, (b) $A'_{\rm a} = 0.22$, (c) $A'_{\rm a} = 0.44$ and (d) $A'_{\rm a} = 0.66$. Note that spot (a) is identical to the spot shown in Fig. 2(b).

For $\phi_{\rm a} = \pi/4$, (Fig. 4b), k_x and k_y become approximately even functions of $A'_{\rm a}$ as expected, since changing the sign of the amplitude is equivalent to rotating the axis by $\pi/2$, apart from a very small contribution from curvature of field. This symmetry is also apparent when comparing the results for $\phi_{\rm a} = 0$ (Fig. 4a) with those for $\phi_{\rm a} = \pi/2$ (Fig. 4c).

By comparing figures 1b, 3b and 4, we conclude that astigmatism is the primary aberration yielding the strongest effect on the transverse stiffnesses k_x and k_y, which are very sensitive to the amplitude $A'_{\rm a}$, again in agreement with the experimental results of Ref. [29]. Fig. 4 shows that the astigmatism axis orientation is also extremely important. This overall message will be of great value in the next two sections, where we undertake the task of performing an absolute calibration of stiffness.

III. MEASURING THE ASTIGMATISM PARAMETERS

A. Experimental procedures

In this section, we present the diagnostic procedures employed for the characterization of optical aberrations present in our typical OT setup. Images of the focused laser spot at different planes across the focal region, shown in Fig. 6, have the elongated form typical of astigmatism (see Fig. 5 for theoretical astigmatic spots). They do not show the characteristic shape of coma (see Fig. 2), which we disregard from now on. As discussed in the previous section, the transverse trap stiffness is extremely sensitive to the astigmatism parameters $A'_{\rm a}$ and $\phi_{\rm a}$ when trapping small spheres. Hence a careful characterization of both astigmatism parameters is essential for undertaking a blind theory-experiment comparison.

Our method is based on the quantitative analysis of the images of the focused laser spot reflected by a plane mirror placed near the focal region, as represented in Fig. 7a. The collimated TEM$_{00}$ Nd:YAG laser beam (wave-

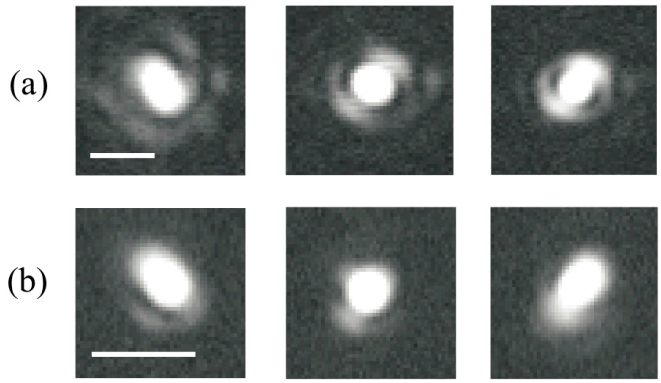

FIG. 6: From left to right, 8-bit laser spot images below, at and above the circle of least confusion. Two different objectives were employed: (a) Plan Apo, NA 1.4, 60X; and (b) Plan Fluor, NA 0.3, 10X. Scale bars (a) 1 μm, (b) 10 μm.

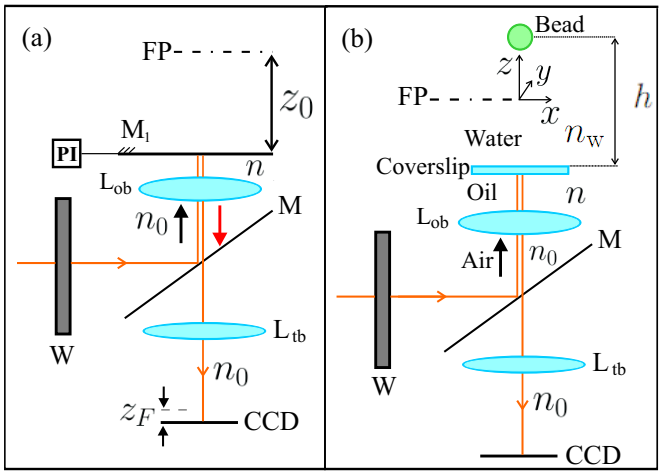

FIG. 7: (Color online) Schematic representation of the experimental setup for (a) characterization of astigmatism; and (b) measurement of the transverse trap stiffness. W = waveplate, M = dichroic mirror; L_{ob} = objective lens; M_1 = laser spot reflecting mirror; PI = piezoelectric controller; FP = objective focal plane; L_{tb} = tube lens; CCD = recording camera.

length $\lambda = 1.064\,\mu$m, waist $w_0 = 4.2$ mm) is transmitted through a waveplate W (quarter or half wavelength) that allows to control its polarization at the back entrance of a Nikon Eclipse TE300 oil-immersion inverted microscope (Nikon, Melville, NY). After partial reflection by the dichroic mirror M (80% reflectivity), the laser beam propagates in air (refractive index n_0) and reaches the objective lens L_{ob} (Nikon PLAN APO, NA 1.4, 60X, aperture radius $R_0 = 5.0 \pm 0.1$ mm and focal distance $f = 0.5$ cm) that focuses the laser beam into a spot localized at the objective focal plane FP in the immersion oil medium of refractive index n. The mirror M_1 (99% reflectivity) at position z_0 reflects the laser beam back towards the objective. On its way back a small fraction of the power is transmitted by the mirror M and the spot image is conjugated by the tube lens L_{tb} (focal distance $f_{tb} = 20$ cm) onto a CCD (charge-coupled device) camera, which records the defocused spot image. We employ the piezoelectric nanopositioning system PI (Digital Piezo Controller E-710, Physik Instrumente, Germany) to move the mirror M_1 across the focal region with controlled velocity $V = 100$ nm/s. Images of the entire process are recorded using a LG7 frame grabber (Scion, USA) connected to a computer.

Typical images are shown in Fig. 6 with (a) the high NA objective used for trapping and (b) a low NA objective. We use (b) to infer the astigmatism phase Φ_s introduced by the set of lenses and mirrors along the optical train between the laser and the objective entrance port in the actual trapping setup, since the optical aberration introduced by a carefully aligned low NA objective is negligible.

On the other hand, the images collected with the high NA objective used for trapping contain the information on the astigmatism phase Φ_{ob} introduced by the objective itself. Since the image is formed after back and forth propagation through the objective, the corresponding total phase is $\Phi_t = 2\Phi_{ob} + \Phi_s$. In short, we measure Φ_s with the help of the low NA objective, and then measure Φ_t with the high NA objective used for trapping. By combining the two results, we infer the total OT astigmatism phase

$$\Phi_{OT} = \Phi_{ob} + \Phi_s \tag{11}$$

for the trapping beam at the sample region, which is the relevant one for the evaluation of the trapping force using the MDSA+ theory presented in Sec. 2.

It is simpler to add the different phases in terms of the Zernike polynomials (origin at the diffraction focus) [31]. To do this, we write the astigmatism phase as $\Phi_{OT}(\rho,\varphi) = 2\pi\, A_{OT}\, (\rho/R_0)^2 \cos[2(\varphi - \phi_{OT})]$ and likewise for Φ_s, Φ_t and Φ_{ob}, in terms of the amplitudes A_s, A_t and A_{ob} and polar angles ϕ_s, ϕ_t and ϕ_{ob}. The connection with the Seidel formalism employed in Sec. 2 is straightforward: we take $A'_a = 2A_{OT}$ and $\phi_a = \phi_{OT}$ and plug the resulting values into the general formalism developed in Sec. 2.

In order to connect the astigmatism phases to the images recorded by the CCD represented in Fig. 7a, we extend the non-paraxial formalism for field propagation developed in [39] to astigmatic spots. This allows us to write the electric field after propagation through the optical elements represented in Fig. 7a in terms of the astigmatism parameters A_t and ϕ_t (when using the high NA objective L_{ob}) or in terms of A_s and ϕ_s (when L_{ob} is replaced by the low NA objective). As in [39], we compute the propagated field to lowest order of f/f_{tb}. In addition, we also assume that mirror M_1 is a perfect reflector and find the electric field at the point (ρ_F, ϕ_F, z_F) in the image space of the tube lens L_{tb} (see Sec. 2.1 for the definitions of the field amplitude E_p and the filling factor γ):

$$\mathbf{E}_{\rm CCD} = -i\frac{E_p k_0 f^2}{f_{\rm tb}} e^{ik_0(f_{\rm tb}-z_F)} e^{2ikf} \int_0^{\theta_0} d\theta \sin\theta\cos\theta e^{-\gamma^2\sin^2\theta} e^{2ikz_0\cos\theta} e^{i\frac{k_0 z_F}{2}\frac{f^2}{f_{\rm tb}^2}\sin^2\theta} \left(g_1^{(+)} + \frac{1}{2}e^{-2i\phi_F} g_1^{(-)}\right) \hat{\mathbf{x}} \quad (12)$$

The astigmatism parameters are contained in the functions $g_m^{(\pm)}(\rho_F, \phi_F, \theta)$ defined in Eq. (8) ($m = 1$). Here we take the coma amplitude to be zero ($A'_{\rm c} = 0$, $\alpha = 0$), in addition to $\mathcal{Z} = k_0\rho_F(f/f_{\rm tb})\sin\theta$ and $A'_{\rm a} = 2A_{\rm t}$, $\phi_{\rm a} = \phi_{\rm t}$. When considering the low NA setup, we take $A'_{\rm a} = 2A_{\rm s}$, $\phi_{\rm a} = \phi_{\rm s}$ and replace θ_0 by the much smaller angular aperture corresponding to NA = 0.3.

We measure the energy density variation with the mirror position z_0 using the CCD and fit the resulting curve with the help of (12) in order to infer the astigmatism amplitudes, as detailed in the next subsection.

B. Results

In Fig. 8a, we plot a typical result for the axial ($\rho_F = 0$) relative energy density, $E^2/E^2_{\rm max}$, as a function of z_0. We fit the experimental data by taking the square modulus of (12). In table 1, we show the results for the fitting parameters $A_{\rm t}$, $E^2_{\rm max}$, z_F, representing the position of the CCD (see Fig. 7a), and the mirror's position offset z' ($z_0 \to z_0 - z'$). Each line in table 1 corresponds to a different measurement. Since the axial energy density does not depend on the astigmatism orientation axis, we are allowed to combine results for different polarization directions here.

measurement	A_t	$E^2_{\rm max}$ (arb. unit)	z_F(cm)	$z'(\mu$m)
1	0.95	2.8	4.9	-8.5
2	0.98	2.7	5.4	-8.8
3	0.99	2.7	5.5	-9.6
4	0.94	2.7	5.3	-9.7
5	0.99	2.5	5.6	-10.7
6	0.91	2.5	4.6	-8.6
7	0.9	2.9	4.9	-8.4
8	0.97	2.6	5.1	-10.0
9	0.97	2.7	4.8	-9.3
10	0.99	2.6	5.1	-9.9

TABLE I: Parameters employed for the curve fit of the relative axial electric energy density (see Fig. 8(a) for a typical example): A_t (astigmatism amplitude), $E^2_{\rm max}$ (maximum energy density), z_F (plane of detection) and z' (offset), for NA = 1.4.

The quality of each fit is extremely sensitive to $A_{\rm t}$: changing $A_{\rm t}$ by only 5% leads to a tenfold increase of χ^2. The astigmatism amplitude, averaged out over the 10 measurements shown in Table I, is $A_{\rm t} = 0.96 \pm 0.02$.

In order to determine the axis directions $\phi_{\rm t}$ and $\phi_{\rm s}$, we take the elongated spots shown in Fig. 6 and fit the contour line corresponding to a given value $E^2_{\rm ctr}$ with an ellipse. The resulting directions do not depend on $E^2_{\rm ctr}$.

measurement	A_t	$E^2_{\rm ctr}$ (arb. unit)	z_F(cm)	$z'(\mu$m)
1	0.85	7.0	5.6	-7.9
2	0.88	8.4	5.6	-8.0
3	0.84	9.1	5.6	-8.0
4	0.93	7.7	5.6	-8.0
5	0.82	8.4	5.4	-7.6
6	0.84	7.7	5.7	-8.2
7	0.83	6.9	5.6	-8.0

TABLE II: Parameters employed for the curve fit of the ratio $R_>/R_<$ between the major and minor semi-axes of the elliptical contour line in the xy plane corresponding to a given electric energy density $E^2_{\rm ctr}$, for the NA=1.4 objective used for trapping (see Fig. 8(b) for a typical example). Same conventions as Table 1.

measurement	A_t	$E^2_{\rm ctr}$ (arb. unit)	$z'(\mu$m)
1	0.25	14.0	4.0
2	0.19	9.2	4.9
3	0.24	6.1	3.3
4	0.22	7.0	4.2

TABLE III: Parameters employed for the curve fit of the ratio $R_>/R_<$ for the NA=0.3 objective used for measuring the system astigmatism (see Fig. 8(c) for a typical example). Same conventions as Table 2.

We find $\phi_{\rm t} = 57^{\rm o} \pm 3^{\rm o}$ and $\phi_{\rm s} = 48 \pm 3^{\rm o}$ for the high (Fig. 6a) and low (Fig. 6b) NA objectives, respectively.

The ellipses also contain information on the values of the astigmatism amplitudes. We consider the ellipse major and minor semi-axes $R_>$ and $R_<$ and plot the ratio $R_>/R_<$ versus z_0 in Figs. 8b (high NA) and 8c (low NA). The ratio varies over a much larger distance range in the second case, as expected in the paraxial regime. We fit the resulting experimental data with a theoretical curve calculated from Eq. (12). For the paraxial low NA objective, we can simplify the angular function in the integrand of (12) and isolate the entire dependence on z_0 and z_F (apart from a trivial phase pre-factor) in terms of the linear combination $-kz_0 + (k_0/2)(f/f_{\rm tb})^2 z_F$. Rather than taking z_F and the offset z' as independent fitting parameters, we set $z_F = 0$ since any finite value of z_F is formally equivalent to a given mirror position offset z' in this case. The results for the fitting parameters are shown in Tables 2 and 3 for the NA 1.4 and NA 0.3 objectives, respectively.

By averaging the values shown in Table 2, we find $A_{\rm t} = 0.86 \pm 0.03$, close to the value found from the axial energy density distribution. Note that any spherical aberration produced by the objective or by the optical components located between the laser output and the objective entrance would modify the axial energy density but not the ratio $R_>/R_<$. Thus, the agreement we

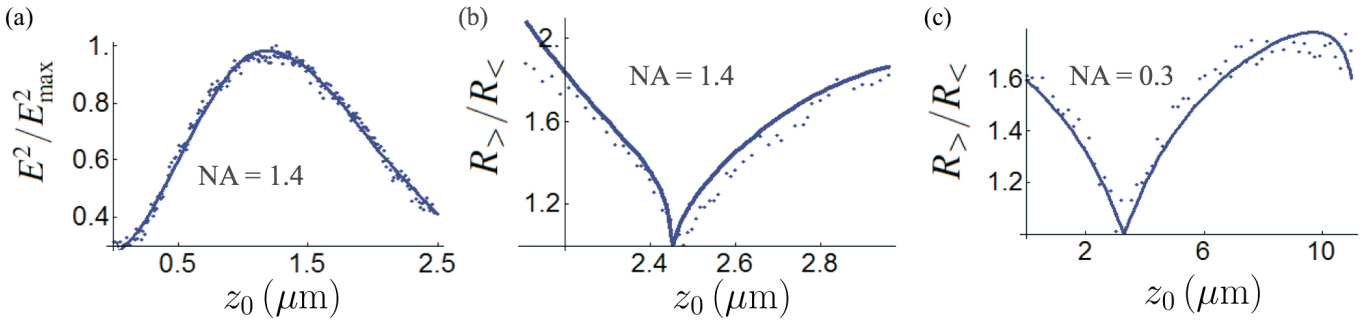

FIG. 8: (Color online) Characterization of astigmatism: experimental data (circles) and curve fit (solid) (a) for the relative axial electric energy density $E^2/E^2_{\rm max}$ versus mirror position z_0 (NA=1.4 objective); for the ratio of spot radii $R_>/R_<$ versus z_0 with (b) NA=1.4 objective and (c) NA=0.3 objective. For the parameters employed in the fits see Tables 1-3.

have found between the two methods shows that system spherical aberration is negligible in the setup shown in Fig. 7a. This was checked by including spherical aberration in Eq. (12) and fitting the spherical aberration amplitude $A_{\rm sa}$ using the axial energy density and the value for $A_{\rm t}$ found from the ratio $R_>/R_<$. The results are distributed around zero with $|A_{\rm sa}| < 0.1$. On the other hand, the interface spherical aberration in the trapping setup (see Fig. 7b) is very important [12] and it is essential to include it in the MDSA+ theoretical model.

We take $A_{\rm t} = 0.92 \pm 0.04$, as the overall average combining the two methods. From Table 3, we find $A_{\rm s} = 0.23 \pm 0.02$ for the system astigmatism. It is not possible to check this value from the axial energy density variation, which is approximately constant in the range of distances covered by the PI, as expected in the paraxial regime. We now combine all these values and solve

$$A_t \cos 2\phi_t = A_s \cos 2\phi_s + 2A_{\rm ob} \cos 2\phi_{\rm ob} \quad (13)$$
$$A_t \sin 2\phi_t = A_s \sin 2\phi_s + 2A_{\rm ob} \sin 2\phi_{\rm ob}. \quad (14)$$

to find the objective parameters $A_{\rm ob} = 0.35 \pm 0.01$ and $\phi_{\rm ob} = (60 \pm 3)^{\rm o}$. We then combine the objective parameters with A_s and ϕ_s in a similar way [see Eq. (11)] and find $A_{\rm OT} = 0.56 \pm 0.03$ and $\phi_{\rm OT} = 55 \pm 3^o$ (a larger astigmatism amplitude was estimated in a similar setup [29]). In the next section, we plug these values into MDSA+ theory and compare the results with the experimental data.

IV. TRANSVERSE STIFFNESS CALIBRATION

A. Experimental Procedures

We validate our proposed absolute calibration by comparison with other known methods [7]. For testing MDSA theory, both Brownian correlations and fluid drag forces were employed as calibration techniques [12], with comparable results. Here we compare MDSA+ with the results obtained by the second approach, with the drag coefficient calculated from Faxén's law [40].

Our experimental procedures also include the measurement of all input parameters relevant for MDSA+. Besides the astigmatism parameters discussed in Sec. III, we also measure the laser beam power and beam waist at the objective entrance port, and the objective transmittance [41], as described in Ref. [12]. Whenever possible, each input parameter was measured by two different techniques, checking the results against each other for consistency.

Our OT setup, illustrated by Fig. 7b, is very similar to the setup for characterization of astigmatism, except for the replacement of mirror M_1 by a glass coverslip at the bottom of our sample chamber containing polystyrene microspheres (Polysciences, Warrington, PA), diluted to 1μl of stock solution 10%v/v in 10 ml of water. In order to determine the amount of spherical aberration introduced by the glass-water planar interface (see Sec. 2.B.1 for details), we first move down the inverted objective until the trapped bead just touches the bottom of the sample chamber. Then we displace the objective upwards through a controlled distance d.

Once the height of the equilibrium position is set, we measure the trap stiffness using Faxén's law [40] and videomicroscopy. We set the microscope stage to move laterally with a measured velocity v [42] either along the x (polarization) or y direction, producing a Stokes drag force βv that displaces the bead off-axis through a distance $\delta\rho$ along the same direction. We calculate β from Faxén's law using the values for the bead radius a and height h. Each run is recorded with a LG7 frame grabber (Scion, USA). From the digitized images of the trapped bead we determine $\delta\rho$ as a function of v. We employ values of v small enough to probe only the linear range of the optical force: $\beta v = k_{x,y}\delta\rho$. We check that our data for the lateral displacement is a linear function of v, $\delta\rho = \alpha v$, determine the coefficient α and then the transverse stiffness $k_{x,y} = \beta/\alpha$ [43]. When comparing with theory, we take the stiffness per unit power $k_{x,y}/P$, where the power at the sample region P is derived from the measured objective transmittance and power at the objective entrance port.

B. Experimental results and comparison with MDSA+

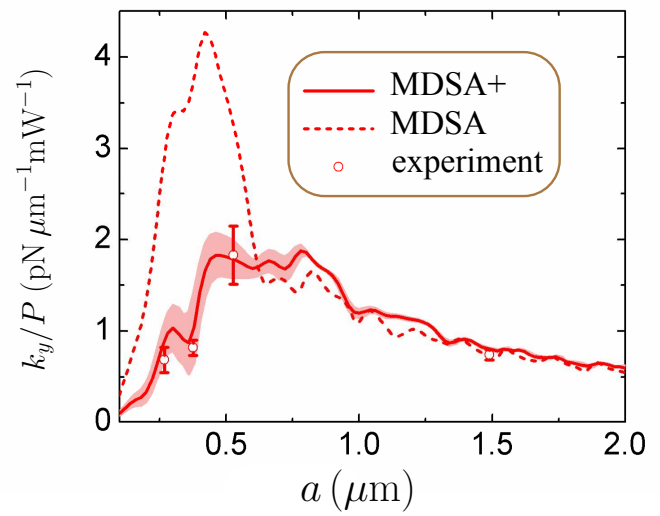

FIG. 9: (Color online) Transverse trap stiffness per unit power k_y/P versus bead radius a for an objective displacement $d = 3.0 \pm 0.5\,\mu$m. No adjustable parameters are employed. Solid line: MDSA+ with the measured astigmatism parameters $A_{\rm OT} = 0.56$ and $\phi_{\rm OT} = 55^{\rm o}$, shaded theoretical uncertainty band bounded by the curves calculated for $A_{\rm OT} \mp \delta A_{\rm OT}$, $\phi_{\rm OT} \pm \delta\phi_{\rm OT}$ and $d = 3.0 \mp 0.5\,\mu$m ($\delta A_{\rm OT} = 0.03$ and $\delta\phi_{\rm OT} = 3^{\rm o}$), circles: experimental results and dashed line: MDSA.

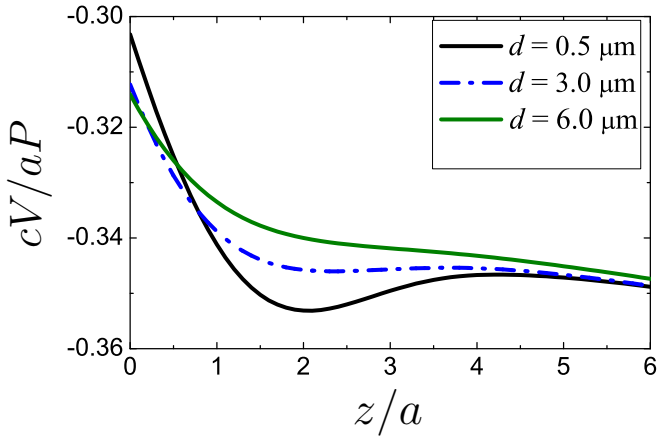

FIG. 10: (Color online) MDSA+ axial potential V (per unit power divided by a/c) versus z/a for $a = 0.376\,\mu$m. The optical potential well becomes shallower as the objective is displaced upwards through the distance d. For d around 3μm, it displays a region of indifferent equilibrium.

In Fig. 9, we plot the transverse stiffness per unit power k_y/P as a function of bead radius a for an objective displacement $d = 3.0 \pm 0.5\,\mu$m. All relevant input parameters are determined independently of the stiffness calibration, and no fitting is implemented in the comparison with the experimental results for the trap stiffness discussed in this section. We calculate with the following parameters: beam waist at the objective entrance port $w_0 = 4.2\,$mm, laser wavelength $\lambda = 1.064\,\mu$m, objective focal length $f = 0.5\,$cm, polystyrene, water and glass refractive indexes $n_{\rm PS} = 1.576$, $n_{\rm w} = 1.332$, and $n = 1.51$, and semi-aperture angle $\theta_m = \sin^{-1}(n_{\rm w}/n) = 61.9^o$. For MDSA+, we also take the measured astigmatism parameters (see Sec. III). Fig. 9 provides an overall assessment of the stiffness behavior as one sweeps the sphere radius from the Rayleigh a^3 increase to the geometrical optics $1/a$ decrease. The MDSA curve (dashed line), corresponding to a stigmatic beam, develops a peak in the range from $\lambda/4$ to $\lambda/2$, at the cross-over between Rayleigh and geometrical optics regimes, in which the stiffness is highly overestimated. Clearly, by including the effect of astigmatism, MDSA+ provides a much better description of the experimental data in this range. On the other hand, the effect of astigmatism is reduced for larger values of a, as expected, since the details of the energy density distribution are averaged out when computing the optical force on a large microsphere. These properties are in qualitative agreement with Ref. [44], where the astigmatism correction was found to be relevant for a microsphere of radius $0.4\,\mu$m but not for large beads.

The width of the theoretical uncertainty band shown in Fig. 9, bounded by the curves corresponding to parameters $A_{\rm OT} \mp \delta A_{\rm OT}$ and $\phi_{\rm OT} \pm \delta\phi_{\rm OT}$, indicates that the sensitivity to astigmatism is larger for small and moderate bead sizes. More generally, the trap becomes more susceptible to perturbations at the crossover between Rayleigh and geometrical optics regimes, as exemplified by the effect of astigmatism discussed here. This is of considerable practical importance, because this region corresponds to the radii most often used in quantitative applications, for which a reliable transverse stiffness calibration is needed.

Right at the center of the MDSA peak region shown in Fig. 9, we observe experimentally that the trap becomes less stable, particularly for larger trap heights. This is well explained by MDSA+. Although the optical force is not conservative [45], we can still define an effective axial potential as the integral of the axial force component along the z axis, in order to interpret the trap stability in a more intuitive way. We find that there is a window of instability for bead radii in the neighborhood of $a = 0.376\,\mu$m as we displace the objective upwards. In Fig. 10, we plot the dimensionless axial potential $cV/(aP)$ versus z/a for $a = 0.376\,\mu$m. The potential well becomes shallower as d increases and no equilibrium is found for $d = 6\,\mu$m. Experimentally, we find a range of approximately indifferent equilibria when $d > 3\,\mu$m, resulting in a large dispersion of the experimental values. This translates into the larger experimental error bars shown in Fig. 11(b), where we plot k_x/P and k_y/P versus objective displacement d. The axial potential well

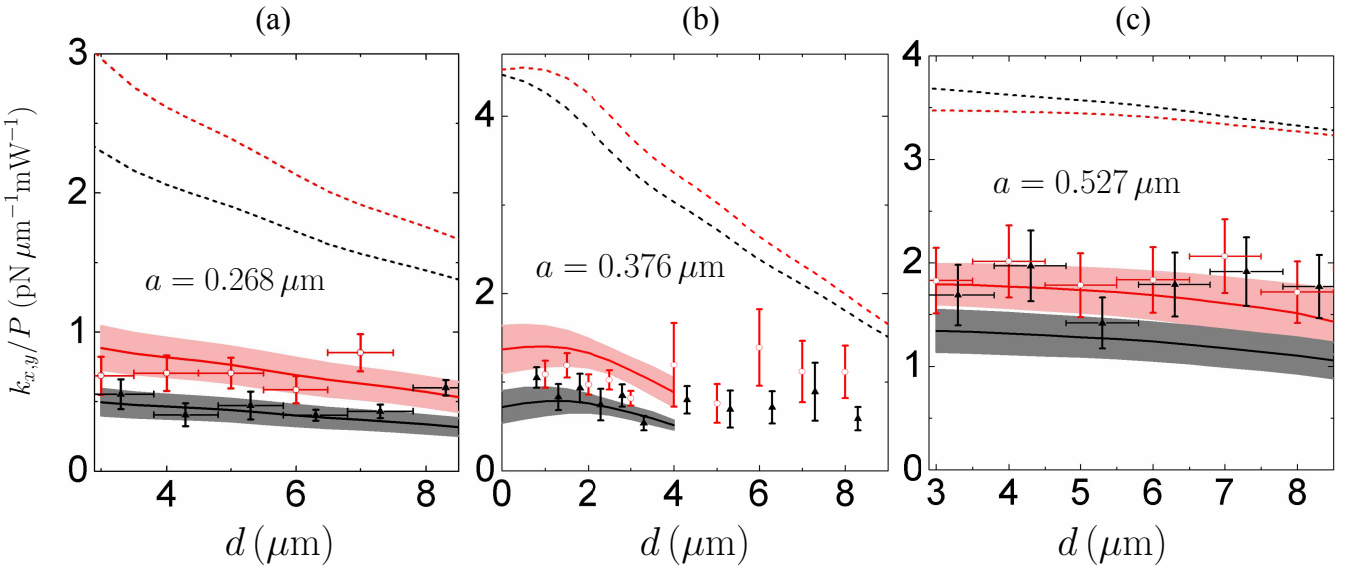

FIG. 11: (Color online) Transverse trap stiffnesses per unit power versus objective vertical displacement d for different microsphere radii: (a) $a = 0.268\,\mu$m, (b) $0.376\,\mu$m and (c) 0.527μm (same conventions as Fig. 9). Black line: k_x/P; red (light gray) line: k_y/P. For clarity, the values of d corresponding to the experimental points for k_x have an offset of $+0.3\,\mu$m, and the horizontal error bars (corresponding to $\delta d = 0.5\,\mu$m) are omitted in plot (b).

is also very shallow for $a = 0.527\,\mu$m, and the large error bars in Fig. 11(c) are again consistent with this property.

Among the three bead sizes presented in Fig. 11, the radius $a = 0.376\,\mu$m right at the instability window is also the one for which we find the largest discrepancy between MDSA and the experimental/MDSA+ values. In this case, MDSA overestimates stiffness by a factor larger than 4 for k_x at low heights and predicts a steady decrease as a function of d which is not observed experimentally. The effect of enhancing the spherical aberration introduced by the glass slide as d increases, which is clearly present in the MDSA curves for the two smaller radii shown in Fig. 11, becomes less severe since the energy density gradient is already degraded by the presence of astigmatism in MDSA+.

Some of the data points shown in Fig. 11(b) correspond to bead heights below $1\,\mu$m. Traps very close to the glass slide can be affected by additional perturbations, not taken into account in MDSA+, including optical reverberation (multiple light scattering between the glass slide and the microsphere), surface interactions and the contribution of evanescent waves beyond the critical angle. The first two effects were carefully probed in Ref. [46]. For a polystyrene bead of radius 0.264μm, an intensity modulation was found for distances below $1\,\mu$m, indicating the interference between the trapping beam and the scattered field reflected by the glass slide. This clearly affects the equilibrium position, but no effect was found on the transverse stiffness calibration [46]. However, larger beads at distances below 3λ from the surface might suffer from a stronger reverberation effect, particularly when considering the axial stiffness.

Fig. 11 shows that k_y is larger than k_x, specially for small spheres, which act as local probes of the electric energy density profile. In the stigmatic case, the focused spot is elongated along the polarization direction [18], as shown in Fig. 5a, thus leading to a larger gradient along the y axis. This can be reversed by a positive astigmatism when the axis orientation is smaller than $\pi/4$ (see Figs. 4 and 5). However, in Fig. 11 we take $\phi_{\rm OT} = 55^{\rm o}$, and as consequence the relative difference between k_y and k_x is actually enhanced by astigmatism, specially for the radius $a = 0.376\,\mu$m. In spite of the large error bars, the experimental data shown in the figure are again consistent with this theoretical prediction.

V. CONCLUSION

Our numerical examples show that even a small amount of astigmatism leads to a measurable reduction of the transverse trap stiffness for microsphere radii in the range between $\lambda/4$ and $\lambda/2$. This is of considerable practical importance, as most quantitative applications rely on transverse stiffness calibrations for microspheres precisely in this range.

From a theoretical point of view, this interval of microsphere radii corresponds to the cross-over between the Rayleigh and ray optics regimes. Fig. 9 provides an overall picture as far as the transverse stiffness is concerned. Right at the crossover, MDSA develops a peak (maximum close to $a = 0.4\,\mu$m for $\lambda = 1.064\,\mu$m), which is severely reduced (and slightly shifted towards larger radii) when astigmatism is included. Therefore, correct-

ing astigmatism, for instance with the help of spatial light modulators [44, 47, 48], might lead in principle to a fourfold increase in the transverse stiffness of our typical OT setup.

Figs. 9 and 11 represent a fair sample of the general good agreement between experimental results and MDSA+ that we have found for a variety of bead sizes and trap heights, for circular as well as for linear polarizations, for the transverse stiffness either along x or y directions (the case of circular polarization was briefly reported in [30]). We have also found qualitative agreement with previous measurements of primary aberrations effects [29, 44].

With our experimental setup, we have independently measured all parameters needed for the explicit numerical computation of the MDSA+ predictions. In particular, the astigmatism parameters were determined using a simple videomicroscopy method, based on the analysis of the reflected focused spot, that can be easily adapted to any OT setup. The success of such a blind theory-experiment comparison demonstrates that MDSA+ can be used as a practical calibration tool, covering the whole range of sizes from the Rayleigh regime to the ray optics one, including the intermediate size interval (peak region) most often employed in applications.

As stated in [12] for MDSA, it remains true that MDSA+ does not include the effects of reverberation (multiple light reflections between the bead and the glass slide), and those of evanescent waves beyond the critical angle. Thus, it is advisable when employing it to stay away from the glass slide by at least a couple of wavelengths. It would be of considerable interest to extend the theory to evanescent wave excitation, so as to provide a theoretical description of fluorescence microscopy of single molecules [49].

Another promising application is the measurement of surface interactions between a microsphere and a plane surface [46] or between two trapped microspheres [50]. Absolute OT calibration allows force measurements, currently under way in our laboratory, down to femtonewtons, with the investigation of Casimir forces as a prospect.

In summary, by taking the primary aberrations into account, MDSA+ provides a complete description of the most often employed OT setup when trapping far from the surface. Astigmatism is the primary aberration that produces the largest effect on the transverse stiffness. In our typical setup, it reduces the stiffness by a large factor and, more importantly, it degrades the trap stability for radii close to or slightly smaller than $\lambda/2$. The instability effect could be even more striking when trapping high-refractive index particles in water [27] or airborne aerosol particles [51], because of the larger radiation pressure contribution in these cases. The achievement of absolute calibration signifies that we now have a satisfactory basic understanding of the performance of OT, bringing about the possibilities of improved design, fuller control and the extension of the usual domain of applicability of these remarkable instruments, ranging from femtonewtons to nanonewtons.

Acknowledgments

We thank B. Pontes and O. N. Mesquita for discussions. We are indebted to the referee for valuable comments. This work was supported by the Brazilian agencies CNPq, FAPERJ and INCT Fluidos Complexos.

Appendix A: Partial-wave series for the dimensionless optical force efficiency

In this appendix, we write the explicit partial-wave series for the cylindrical components of the dimensionless optical force efficiency $\mathbf{Q}$ defined by eq. (5).

$\mathbf{Q}$ contains two separate contributions: $\mathbf{Q} = \mathbf{Q}_e + \mathbf{Q}_s$. The extinction contribution $\mathbf{Q}_e$ represents the rate at which momentum is removed from the focused incident beam. $\mathbf{Q}_s = \mathbf{Q}_s^{(\mathrm{p})} + \mathbf{Q}_s^{(\mathrm{c})}$ represents the negative of the rate at which momentum is carried away by the field scattered by the microsphere (Mie scattering). Hence $\mathbf{Q}_s$ is quadratic in the scattered field, with $\mathbf{Q}_s^{(\mathrm{p})}$ containing pure electric (magnetic) multipole contributions, quadratic in the Mie coefficients a_j (b_j) [33], and $\mathbf{Q}_s^{(\mathrm{c})}$ accounting for the cross terms proportional to $a_j b_j^*$. Their cylindrical components are given by partial-wave (multipole) sums of the form

$$\sum_{jm\sigma} \equiv \sum_{j=1}^{\infty} \sum_{m=-j}^{j} \sum_{\sigma=\pm 1} .$$

We find

$$Q_{s\rho}^{(\mathrm{p})} = \frac{2\gamma^2}{AN} \sum_{jm\sigma} \frac{\sqrt{j(j+2)(j+m+1)(j+m+2)}}{j+1} \mathrm{Im}\Big\{ (a_j a_{j+1}^* + b_j b_{j+1}^*) \Big[G_{j,m}^{(\sigma)} G_{j+1,m+1}^{(\sigma)*} + G_{j,-m}^{(\sigma)} G_{j+1,-(m+1)}^{(\sigma)*} \Big] + (a_j a_{j+1}^* - b_j b_{j+1}^*) e^{2i\sigma\phi} \Big[G_{j,m}^{(\sigma)} G_{j+1,m+1}^{(-\sigma)*} + G_{j,-m}^{(\sigma)} G_{j+1,-(m+1)}^{(-\sigma)*} \Big] \Big\} \quad \text{(A1)}$$

$$Q_{s\rho}^{(\mathrm{c})} = -\tfrac{4\gamma^2}{AN}\textstyle\sum_{jm\sigma}\tfrac{(2j+1)}{j(j+1)}\sigma\sqrt{(j-m)(j+m+1)}\ \Big[\mathrm{Re}(a_j b_j^*)\mathrm{Im}(G_{j,m}^{(\sigma)}G_{j,m+1}^{(\sigma)*}) + \mathrm{Im}(a_j b_j^*)\mathrm{Re}(e^{2i\sigma\phi}G_{j,m+1}^{(\sigma)}G_{j,m}^{(-\sigma)*})\Big] \tag{A2}$$

$$Q_{sz}^{(\mathrm{p})} = -\frac{4\gamma^2}{AN}\mathrm{Re}\sum_{jm\sigma}\frac{\sqrt{j(j+2)(j+m+1)(j-m+1)}}{j+1} \times\Big[(a_j a_{j+1}^* + b_j b_{j+1}^*)G_{j,m}^{(\sigma)}G_{j+1,m}^{(\sigma)*} + (a_j a_{j+1}^* - b_j b_{j+1}^*)e^{2i\sigma\phi}G_{j,m}^{(\sigma)}G_{j+1,m}^{(-\sigma)*}\Big] \tag{A3}$$

$$Q_{sz}^{(\mathrm{c})} = -\frac{4\gamma^2}{AN}\mathrm{Re}\sum_{jm\sigma}\frac{(2j+1)}{j(j+1)}m\sigma a_j b_j^*\left(|G_{j,m}^{(\sigma)}|^2 - e^{2i\sigma\phi}G_{j,m}^{(\sigma)}G_{j,m}^{(-\sigma)*}\right). \tag{A4}$$

$G_{jm}^{(\sigma)}(\rho,\phi,z)$ are the focused beam multipole coefficients in the case of a circularly polarized beam at the objective entrance (helicity σ), defined by eq. (6). The cross terms of the form $G_{j,m}^{(\sigma)}G_{j',m'}^{(-\sigma)*}$ in (A1)-(A4) arise from writing the the linearly-polarized field as a superposition of $\sigma = \pm 1$ circular polarizations and squaring the resulting scattered field when computing the stress tensor. Thus, they are absent in the case of circular polarization discussed in Ref. [30]. The filling factor A appearing in (A1)-(A4) represents the fraction of laser bem power transmitted through the objective aperture and the glass-slide [52]:

$$A = 16\gamma^2\int_0^{\theta_m} ds\, s\, \exp(-2\gamma^2 s^2)\,\frac{\sqrt{(1-s^2)(N^2-s^2)}}{(\sqrt{1-s^2}+\sqrt{N^2-s^2})^2} \tag{A5}$$

The azimuthal component contributions $Q_{s\phi}^{(\mathrm{p})}$ and $Q_{s\phi}^{(\mathrm{c})}$ are given by expressions similar to (A1) and (A2), respectively. The dimensionless extinction force cylindrical components are given by

$$Q_{e\rho} = \frac{\gamma^2}{AN}\mathrm{Im}\sum_{jm\sigma}(2j+1)G_{j,m}^{(\sigma)}\Big[(a_j+b_j)\left(G_{j,m+1}^{-,(\sigma)} - G_{j,m-1}^{+,(\sigma)}\right)^* + (a_j-b_j)e^{2i\sigma\phi}\left(G_{j,m+1}^{-,(-\sigma)} - G_{j,m-1}^{+,(-\sigma)}\right)^*\Big] \tag{A6}$$

$$Q_{ez} = \frac{2\gamma^2}{AN}\mathrm{Re}\sum_{jm\sigma}(2j+1)G_{j,m}^{(\sigma)}\left[(a_j+b_j)G_{j,m}^{C,(\sigma)*} + (a_j-b_j)e^{2i\sigma\phi}G_{j,m}^{C,(-\sigma)*}\right] \tag{A7}$$

The series representing $Q_{e\phi}(\rho,\phi,z)$ is similar to (A6).

In addition to the multipole coefficients $G_{j,m}^{(\sigma)}$ defined by Eq. (6), we have also defined

$$G_{j,m}^{C,(\sigma)}(\rho,\phi,z) = \int_0^{\theta_m} d\theta\sin\theta\cos\theta_{\mathrm{w}}\sqrt{\cos\theta}\,e^{-\gamma^2\sin^2\theta}T(\theta)d_{m,\sigma}^{j}(\theta_{\mathrm{w}})g_m^{(\sigma)}(\rho,\phi,\theta) \times\exp\left\{i[\Phi_{\mathrm{g-w}}(\theta)+\Psi_{\mathrm{add}}(\theta)+k_{\mathrm{w}}\cos\theta_{\mathrm{w}}z]\right\} \tag{A8}$$

$$G_{j,m}^{\pm,(\sigma)}(\rho,\phi,z) = \int_0^{\theta_m} d\theta\sin\theta\sin\theta_{\mathrm{w}}\sqrt{\cos\theta}\,e^{-\gamma^2\sin^2\theta}T(\theta)d_{m\pm1,\sigma}^{j}(\theta_{\mathrm{w}})g_m^{(\sigma)}(\rho,\phi,\theta) \times\exp\left\{i[\Phi_{\mathrm{g-w}}(\theta)+\Psi_{\mathrm{add}}(\theta)+k_{\mathrm{w}}\cos\theta_{\mathrm{w}}z]\right\}. \tag{A9}$$

Appendix B: A short guide to absolute calibration

An important application of absolute calibration is the possibility of designing the optical trap to meet some specific requirement. The parameters required for the deter-

mination of the trap stiffness [53] include the microsphere radius a and refractive index, the laser wavelength λ (in vacuum) and power at the objective entrance port, the refractive indexes of the glass slide n and of the liquid filling the sample $n_{\rm w}$ (water in many cases), and the objective numerical aperture NA and transmittance. All these parameters are usually readily available, except for the last one, which can be reliably measured by the dual objective method [41], or by using a mercury microdroplet as a microbolometer [54].

One can enlarge the beam waist w_0 so as to increase the trapping stability region by overfilling the objective entrance port. In a given setup, w_0 can be inferred by measuring the laser power transmitted through a diaphragm as a function of its radius, or alternatively by imaging the laser beam spot with a CCD [12].

Once these basic input parameters are known, the path to absolute calibration depends on the ratio a/λ as follows:

- $a < \lambda$. Astigmatism and interface spherical aberration should be taken into account. The latter is controlled by starting with the trapped bead at the very bottom of the sample. One then displaces the objective by a given amount d. Our code [53] calculates the resulting spherical aberration effect. Since we neglect reverberation and the contribution of evanescent wave components, reliable results are expected in the range $d > 3\lambda$.

  When trapping the small microspheres typically employed in quantitative applications, it is also essential to characterize the astigmatism axis orientation and amplitude. For instance, for $a/\lambda \sim 0.25$, Fig. 4 shows that a small amount of astigmatism leads to a significant reduction of the transverse stiffness.

  By imaging the reflected laser spot in a CCD, it is straightforward to measure the axis orientation. The amplitude can be derived by fitting the variation of the intensity at the spot center with the position of the mirror (see Sec. III for details).

- $\lambda < a < 2\lambda$. For bead radii $a > \lambda$, the effect of astigmatism on the trap stiffness is small (see Fig. 9). Thus, depending on the required accuracy, the stiffness can be calculated using our code as if the trapping beam were stigmatic. Moreover, the dependence on d is also negligible provided that the bead is trapped far from the glass surface.

- $a > 2\lambda$. Our code is not optimized for very large radii, so we do not recommend its use in this case. On the other hand, geometrical optics provides an excellent approximation to the transverse stiffness in this range. In this regime, the stiffness is virtually independent of wavelength, polarization and trapping height (again as long as reverberation is negligible): $k_{x,y}/P = C/a$, with the coefficient C independent of a. For overfilled oil-immersion high-NA objectives, we find [26] $C = 1.1\,\mathrm{pN}/(\mu\mathrm{m}\cdot\mathrm{mW})$ (with a measured in μm) in the most common case of polystyrene beads in water.

[1] A. Ashkin *et al.*, Opt. Lett. **11**, 288 (1986).
[2] A. Ashkin, *Optical Trapping and Manipulation of Neutral Particles Using Lasers: A Reprint Volume With Commentaries* (World Scientific, Singapore, 2006).
[3] S. Toyabe *et al.*, Nature Physics **6**, 988 (2010).
[4] A. Brut *et al.*, Nature **483**, 187 (2012).
[5] C. Bustamante *et al.*, Cell **144**, 480 (2011).
[6] F. M. Fazal and S. M. Block, Nature Photonics **5**, 318 (2011).
[7] K. C. Neuman and S. M. Block, Rev. Sci. Instrum. **75**, 2787 (2004).
[8] R. Simmons *et al.*, Biophys. J. **70**, 1813 (1996).
[9] K. Berg-Sørensen and H. Flyvbjerg, Rev. Sci. Instrum. **75**, 594 (2004).
[10] S. F. Tolić-Nørrelykke *et al.*, Rev. Sci. Instrum. **77**, 103101 (2006).
[11] B. Pontes *et al.*, Biophys. J. **101**, 43 (2011).
[12] N. B. Viana *et al.*, Phys. Rev. E **75**, 021914 (2007).
[13] G. Roosen, Can. J. Phys. **57**, 1260 (1979)
[14] A. Ashkin, Biophys. J. **61**, 569 (1992).
[15] G. Gouesbet *et al.*, J. Opt. (Paris) **16**, 83 (1985).
[16] J. P. Barton and D. R. Alexander, J. Appl. Phys. **66**, 2800 (1989).
[17] D. Ganic *et al.*, Opt. Express **12**, 2670 (2004).
[18] B. Richards and E. Wolf, Proc. R. Soc. London A **253**, 358 (1959).
[19] P. Debye, Ann. D. Phys. (Lpz) **30**, 755 (1909).
[20] P. A. Maia Neto and H. M. Nussenzveig, Europhys. Lett. **50**, 702 (2000).
[21] M. Guillon, K. Dholakia and D. McGloin, Opt. Express **16**, 7655 (2008).
[22] M. Berry and K. E. Mount, Rep. Prog. Phys. **35**, 315 (1972).
[23] A. Mazolli *et al.*, Proc. R. Soc. London A **459**, 3021 (2003).
[24] P. Török *et al.*, J. Opt. Soc. Am. A **12**, 325 (1995).
[25] N. B. Viana *et al.*, Appl. Phys. Lett. **88**, 131110 (2006).
[26] R. S. Dutra *et al.*, J. Opt. A **9**, 221 (2007).
[27] A. van der Horst *et al.*, Appl. Opt. **47**, 3196 (2008).
[28] D. R. Burnham and D. McGloin, J. Opt. Soc. Am. B **28**, 2856 (2011).
[29] Y. Roichman *et al.*, Appl. Opt. **45**, 3425 (2006).
[30] R. S. Dutra, *et al.*, Appl. Phys. Lett. **100**, 131115 (2012).
[31] M. Born and E. Wolf, *Principles of Optics* (Pergamon Press, Oxford, 1959), ch. IX.
[32] A. R. Edmonds, *Angular Momentum in Quantum Mechanics* (Princeton University Press, Princeton, 1957).
[33] C. F. Bohren and D. R. Huffman, *Absorption and Scatter-*

ing of Light by Small Particles (Wiley, New York, 1983), ch. 4.
[34] G. N. Watson, *A treatise on the theory of Bessel functions* (Cambridge University Press, London, 1966), p. 358.
[35] O. Farsund and B. U. Felderhof, Physica A **227**, 108 (1996).
[36] K. C. Neuman, E. A. Abbondanzieri and S. M Block, Optics Lett. **30**, 1318 (2005).
[37] F. Merenda *et al.*, Opt. Express **14**, 1685 (2006).
[38] The displacement theorem [31] is exact only in the paraxial limit. Within the non-paraxial formalism developed here, curvature of field leads to a very small modification of stiffness, and thereby to a small violation of the symmetry property discussed here.
[39] L. Novotny *et al.*, Opt. Lett. **26**, 789 (2001).
[40] H. Faxén, Annalen der Physik **373**, 89 (1922); M. I. M. Feitosa and O. N. Mesquita, Phys. Rev. **A 44**, 6677 (1991).
[41] H. Misawa *et al.*, J. App. Phys. **70**, 3829 (1991); N. B. Viana *et al.*, Appl. Opt. **45**, 4263 (2006).
[42] An independent measurement of the stage velocities employed in the calibration yielded a systematic error of +9.7% with respect to the nominal values [43]. Thus, the results for the Stokes trap stiffness calibration reported in [30] should be corrected by the same factor. The results presented in Figs. 9 and 11 are derived from the correct values for the stage velocity.
[43] See Supplemental Material for a detailed description of the calibration based on the fluid drag force.
[44] K. Wulff *et al.*, Opt. Express **14**, 4170 (2006).
[45] Y. Roichman *et al.*, Phys. Rev. Lett. **101**, 128301 (2008); G. Pesce *et al.*, Europhys. Lett. **86**, 38002 (2009).
[46] E. Schäffer, S. F. Tolić-Nørrelykke and J. Howard, Langmuir **23**, 3654 (2007).
[47] C. Lopez-Quesada *et al.*, Appl. Opt. **48**, 1084 (2009).
[48] A. Arias *et al.*, Opt. Express **21**, 102 (2013).
[49] M. J. Lang, P. M. Fordyce and S. M. Block, J. Biology **2**, 6 (2003).
[50] D. E. Masri *et al.*, Soft Matter **7**, 3462 (2011).
[51] D. R. Burnham and D. McGloin, Opt. Express **14**, 4175 (2006); K. J. Knox *et al.*, J. Opt. Soc. Am. B **27**, 582 (2010).
[52] The actual objective transmittance must be measured independently when evaluating the power in the sample region [41].
[53] See Supplemental Material for a Mathematica® notebook file that calculates the transverse trap stiffness as a function of the objective upward displacement d using MDSA+.
[54] N. B. Viana, O. N. Mesquita, and A. Mazolli, Appl. Phys. Lett. **81**, 1765 (2002).